J. Wind Eng. Ind. Aerodyn. 142 (2015) 272–288

Contents lists available at ScienceDirect

Journal of Wind Engineering and Industrial Aerodynamics

journal homepage: www.elsevier.com/locate/jweia

An intercomparison study between RAMS and CRES-Flow-NS models and evaluation with wind tunnel experimental data: Toward improving atmospheric modeling for wind resource assessment

Nicolas Barranger [a], Thomas Ternisien [b], George Kallos [a,*]

[a] University of Athens, School of Physics, Division of Applied Physics, Atmospheric Modeling and Weather Forecasting Group, University Campus, Bldg. PHYS-V, 15784 Athens, Greece

[b] Centre for Renewable Energy Sources and Saving (CRES), Pikermi 19009, Greece

ARTICLE INFO

Article history:
Received 30 December 2014
Received in revised form
1 April 2015
Accepted 3 April 2015

Keywords:
Computational fluid dynamics
Mesoscale models
Turbulence closure schemes
Turbulent kinetic energy

ABSTRACT

The use of atmospheric models for wind resource assessment in complex terrain is limited by their coarse resolution. Using non-hydrostatic mesoscale models such as RAMS, fine resolution grids and a proper turbulent closure scheme such as the k–ε, it is theoretically possible to describe orographic shear-induced turbulence at microscale level with certain accuracy. In such cases, microscale CFD models modified to represent the interaction of the atmospheric boundary layer with the local orography are proven to show accurate results in idealized cases such as neutral stratification. On the other hand, their limitation in representing real atmospheric interaction between large scale structures and thermal stratification with the flow pattern can introduce significant errors in evaluating wind energy potential. In this work, proper modifications of the RAMS model were performed to simulate 2D wind flow over an isolated hill at high resolution configuration. The results have been compared with the CFD model CRES-Flow-NS and with wind tunnel experimental data. It is found that RAMS is able to reproduce basic flow features with comparable accuracy as the CFD model. This work is part of a major effort to make RAMS a reliable tool for atmospheric flow simulations of various complexity.

1. Introduction

Wind energy already occupies a considerable portion of the totally produced electric energy in many countries and its use will probably continue to increase in the future. Site selection becomes more and more complicated because of the lack of appropriate areas (the best areas have already been occupied) and imposed limitations. Therefore, there is a need for accurate analysis and forecasting of the wind field at both small and large scale on a continuous manner. Useful tools for such analysis and prediction are the so-called Mesoscale Models (MM), that are usually designed to cover atmospheric motions ranging from synoptic and regional to small scale. In both wind resource mapping and short term power forecasting, this asset allows wind speed and direction estimations with resolution ranging from tens of kilometers to the order of kilometer.

In regions of complex terrain, one of the major modeling issues is the coarse horizontal resolution of MM compared with the characteristic length scale of the orography. Using one and two dimensional Fast Fourier Transform (FFT) to quantitatively estimate the characteristic length scale of local orography, a strong correlation between model accuracy and the level of topography details the model explicitly resolves was proven (Young and Pielke, 1983; Salvador et al., 1998). In highly complex terrain, the characteristic length scale of hills and ridges can be on the order of meters. On the other hand, MM are horizontally averaging the orography details with a characteristic length scale of less than a kilometer. As a direct consequence, the wind flow pattern is locally averaged. This can lead to significant errors in areas subject to local speed-up, detachment and recirculation. In wind resource assessment and wind forecast, several methods have been proposed to tackle this problem.

If meteorological masts (or other instruments) monitoring wind speed and direction are available on-site, statistical methods can significantly improve wind power forecasting. Model Output Statistics (MOS) (Landberg, 1994; Joensen et al., 1999; Von Bremen, 2007; Chen et al., 2013) reduces systematic bias using correction methods that not only take into account the local effect of topography and roughness but also seasonal variability. Kalman filtering techniques provide considerable improvement when Numerical Weather Prediction (NWP) models face weather changes. They

* Corresponding author.
E-mail address: kallos@mg.uoa.gr (G. Kallos).

http://dx.doi.org/10.1016/j.jweia.2015.04.003
0167-6105/

can help in reducing systematic errors but do not necessarily eliminate phase differences (e.g. ramping effect) as discussed in Louka et al. (2008). Although, these methods can be sufficiently accurate in many sites and for most of the time, continuous high quality datasets are always required (Kalnay, 2002). In general, MM output correction methodologies are of reduced accuracy in case where the model output does not exhibit a systematic error trend (model deviation from observations) according to Galanis et al. (2006).

For wind resource mapping, the classical method is to combine measurement available close to the location of interest with microscale models. This allows a better understanding of the spatial variability of the wind in the area under consideration. Two major families of flow solvers are generally used in such cases. In the first one, we find the models based on the linear theory (Jackson and Hunt, 1975; Taylor, 1976; Troen, 1989). They are well known for their low computational resources requirements. However they face some difficulties in resolving detached flows in sharp hill context. In the second one, we find the so called microscale Computational Fluid Dynamics models (CFD). They use iterative pressure solvers such as the Semi-Implicit Method for the Pressure Linked Equations (SIMPLE) (Patankar and Spalding, 1972). Although they were firstly designed to resolve engineering-type of flow-problems, they have been modified to simulate the Atmospheric Boundary Layer (ABL) interacting with complex topography (Apsley and Castro, 1997). In terms of conception, CFD models used in wind flow problems are generally designed to simulate idealized steady-state logarithmic flow profiles and their variation in space according to the terrain variability. The simulations are usually done for several wind directions.

Instead of employing recorded data as an input, microscale models can use MM data. This coupling technique incorporates significant errors due to MM prediction errors mentioned above and the lack of physical representation in microscale models. In fact, most of the microscale models only take into consideration the orography but not the thermal stratification or any other dynamic/thermodynamic processes (low level jets, convection, etc.). Despite these problems the combined application of MM with CFD models is a methodology used more and more during the last decade in wind energy studies (Gopalan et al., 2014).

As computer resources have been exponentially increasing the last decade and terrain characterization datasets are available at very fine scale, state-of-the-art non-hydrostatic atmospheric models are now theoretically capable of resolving mean flow turbulent characteristics at very fine scales. This feature makes possible the study of wind flow pattern in complex terrain at a wind farm scale only by utilizing MM. As an example, Beaucage et al. (2011) used the Advanced Regional Prediction System (ARPS) to simultaneously simulate mesoscale and microscale wind flow pattern with a resolution of 90 m. Marjanovic et al. (2014) studied simple and complex terrain cases with a resolution of 300 m for wind energy forecasting. Obviously, there are certain advantages of using MM in high-resolution configuration. They are transient flow solvers aimed at reproducing real atmospheric conditions. They take into account thermal effects, moisture, radiation budget, Coriolis force, and for the most advanced models, chemical processes, cloud microphysics and detailed landscape characteristics (e.g. vegetation, soil texture) (Pielke, 2013).

MM such as the Weather and Research Forecasting Model (WRF) (Michalakes et al., 2004), ARPS (Xue et al., 2000, 2001) and the Regional Atmospheric Modeling System (RAMS) (Pielke et al., 1992; Cotton et al., 2003) combine two-way interactive nesting capabilities and a terrain following coordinate system to study the wind flow pattern at very fine scale. To prove that RAMS solver was able to simulate small scale flow features in complex terrain, Ying et al. (1994, 1995, 1997) developed and tested a set of second order turbulent closure schemes in RAMS, Trini Castelli and Reisin (2010) used RAMS to study the flow over a single building. Using the two-way interactive nesting capabilities of RAMS, De Wekker et al. (2005) studied the ABL in mountainous regions.

A critical aspect when dealing with microscale turbulent flows is the turbulent closure scheme. In most MM first order closure schemes such as the Mellor Yamada (1982) Level 2.5 (MY25) is used for computing vertical diffusion fluxes of momentum. Furthermore, a local deformation scheme describes horizontal mixing (Smagorinsky, 1963). This configuration allows the computation of Reynolds stresses in a decoupled and anisotropic way with vertical grid spacing being much smaller than the horizontal one. From a numerical point of view, the large size of the horizontal grids allows the computation of the Reynolds stress with non-symmetrical assumption that is necessary to avoid the presence of additional fictitious torque. This closure scheme cannot be used when the terrain variability requires small horizontal grids to explicitly resolve the wind flow pattern. Also, this turbulent closure fails in

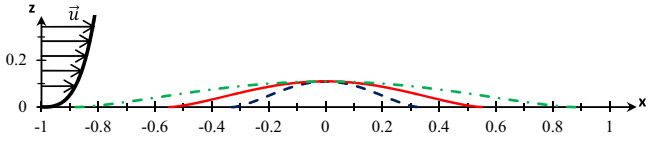

Fig. 1. Hill aspect ratio at wind tunnel scale (in meters): H3 is represented with the blue dashed curve, H5 with the red solid line, H8 with the green dashed dot line and wind flow logarithmic profile. (For interpretation of the references to color in this figure legend, the reader is referred to the web version of this article.)

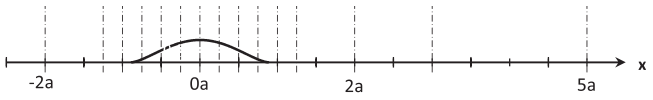

Fig. 2. Wind tunnel measurement locations along the longitudinal axis.

Table 1
Principle differences between the RAMS model and CRES-Flow-NS.

	RAMS	CRES-Flow-NS
Solver	Compressible, density-based	Incompressible, pressure correction method
Numerical method	Explicit	Implicit
Time integration	Second order leapfrog	None (steady state)
Vertical coordinate system	Sigma terrain following	Curvilinear body-fitted
Computer time for identical grid (single CPU intel i7)	12 h wall clock for one hour real event	8 h (after obtaining convergence criteria)
Discretization method	Finite difference	Finite volume
Grid structure	"Staggered" Arakawa C grid	Velocity components "staggered" at grid points. Pressure located at mid-cells
Grid nesting	Two-way interactive nesting	None
Advection discretization method	Second order leapfrog	Second order Total Variation Diminishing (TVD)
Dimensions	3D with option 2D	3D and quasi-3D

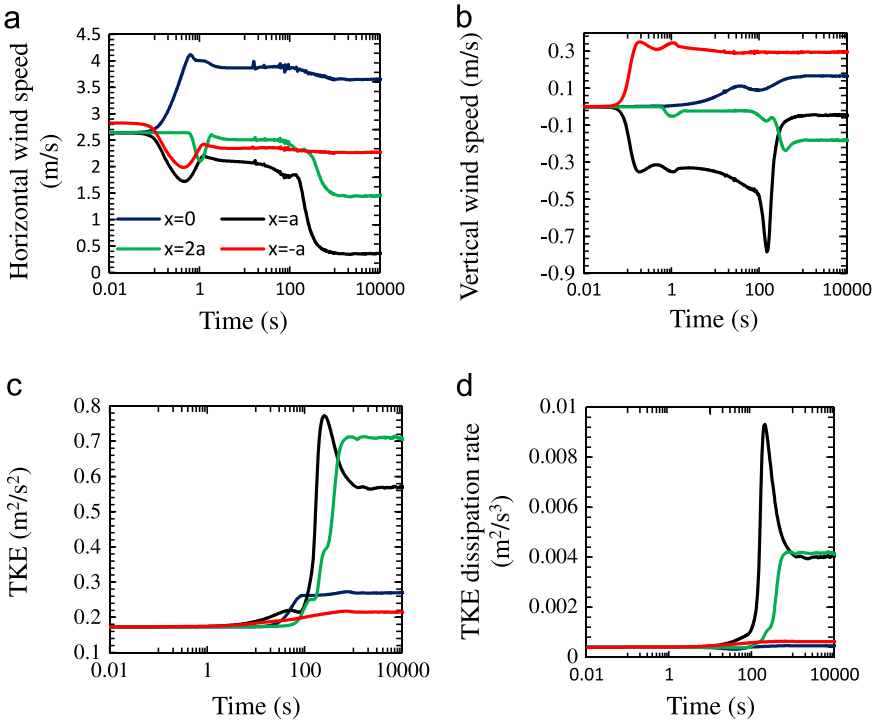

Fig. 3. (a and b) Wind speed components, (c) TKE and (d) TKE dissipation rate variation in time at 20 m above the ground for hill H3 at $x=-a$ (red), $x=0$ (blue), $x=a$ (black) and $x=2a$ (green) with $a=3$ h (hill H3). (For interpretation of the references to color in this figure legend, the reader is referred to the web version of this article.)

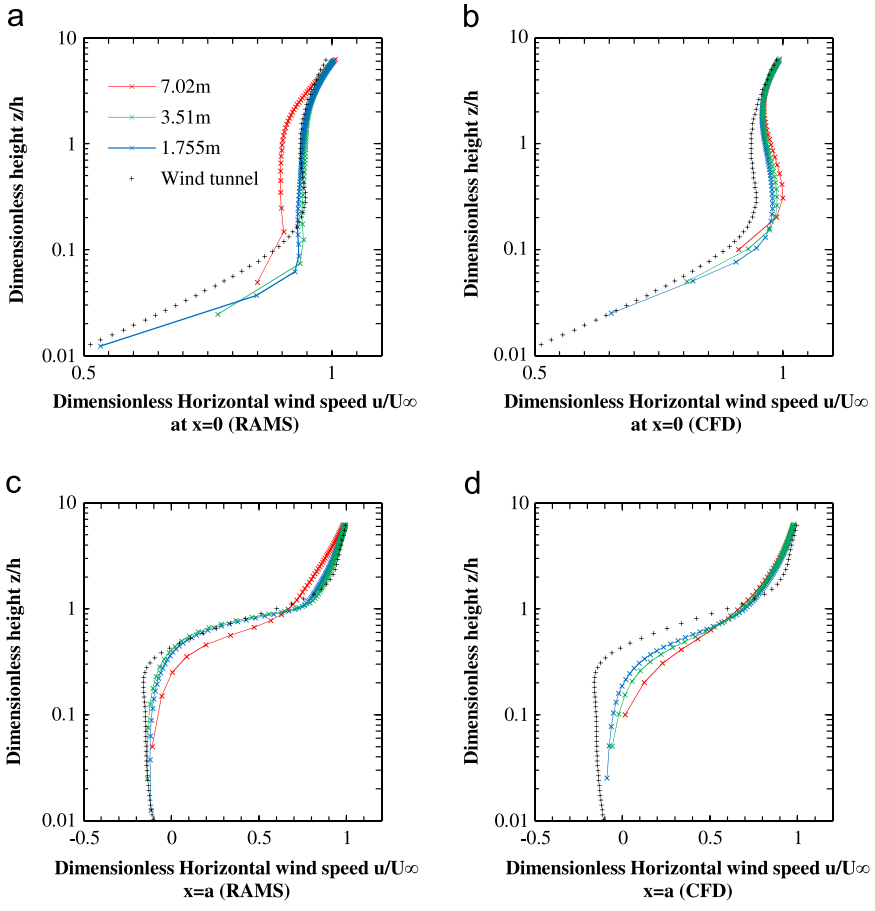

Fig. 4. Dimensionless horizontal wind speed component for hill H3 at hill top simulated with (a) RAMS, (b) CRES-Flow-NS, in the detachment region at $x=1a$ simulated with (c) RAMS, (d) CRES-Flow-NS with vertical grid size being 7.02 m (red), 3.51 m (green) and 1.755 m (blue). Black crosses are wind tunnel measurements. (For interpretation of the references to color in this figure legend, the reader is referred to the web version of this article.)

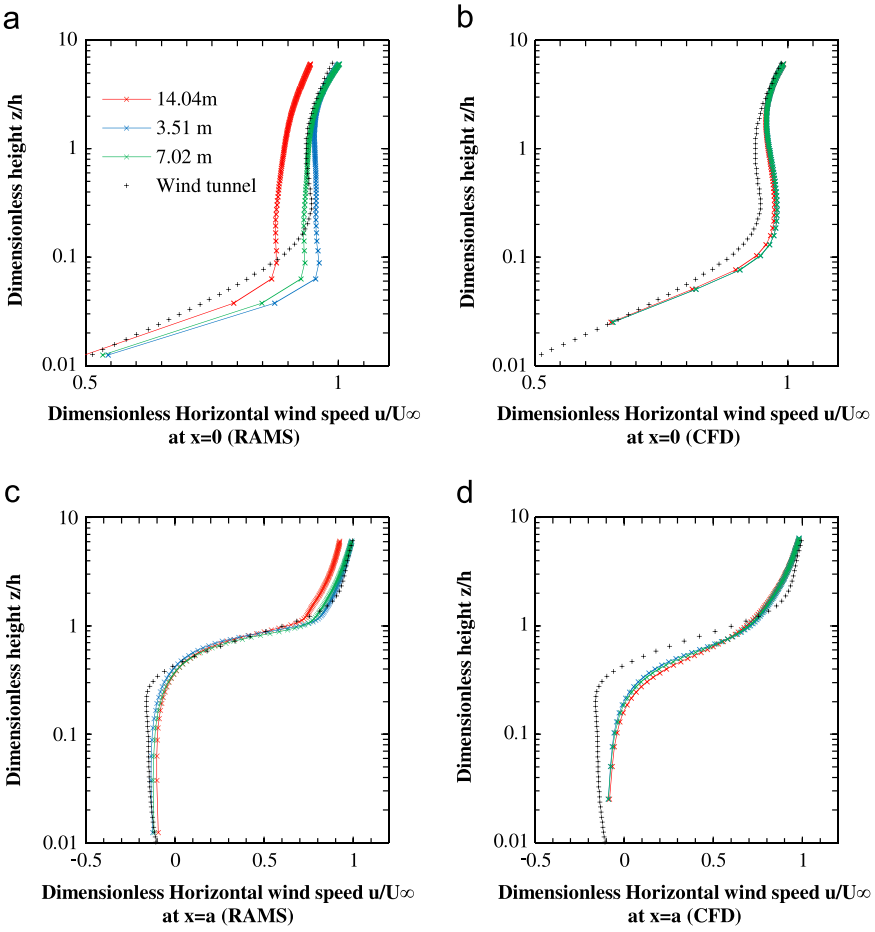

Fig. 5. Dimensionless horizontal wind speed component for hill H3 at hill top simulated with (a) RAMS, (b) CRES-Flow-NS, in the detachment region at $x=1a$ simulated with (c) RAMS, (d) CRES-Flow-NS. The horizontal grid size is 14.04 m (red), 7.02 m (green) and 3.51 m (blue). Black crosses are wind tunnel measurements. (For interpretation of the references to color in this figure legend, the reader is referred to the web version of this article.)

solving Turbulent Kinetic Energy (TKE) even in gentle slope cases (Trini Castelli et al., 2001).

If small scale turbulent motions require being accurately computed, methods estimating the Reynolds stress tensor with the isotropic assumption are necessary. Simulating turbulence in stratocumulus-capped mixed layers, Deardorff (1980) proposed a turbulent closure scheme that explicitly resolves large eddies and parameterizes small scale features. This method, so-called Large Eddy Simulation (LES) is aiming at filtering the wind spectrum according to their scale. Using several filtering techniques, the energy containing eddies are retained into the prognostic equations while the smaller ones are parameterized. In general, this family of turbulence closure schemes is showing promising results (Mirocha et al., 2010). Some recent work has been done on improved filtering techniques (Lundquist et al., 2012). This work has been applied in idealized cases over complex terrain (Chow and Street, 2009). Porté-Agel et al. (2011) performed a similar study but focused on wind turbine farms. Despite this fact, this technique still requires further development and of course validation. In general this approach needs large amount of computer resources.

In wind energy applications, turbulent closure schemes featuring linear eddy viscosity models are commonly used. In MM, their use relies on the Reynolds assumption (Pielke, 2013). For microscale CFD models their applicability is made possible after deriving the Reynolds Averaged Navier Stokes (RANS) equations. They are based either on the one dynamical equation model (Taylor, 1976) or two equations such as k–ε (Launder and Spalding, 1972) and k–ω (Wilcox, 1988). All these models have a prognostic equation for solving the TKE. The k–l model uses a parameterization for the turbulent length scale (Blakadar, 1962) while k–ε and k–ω use a second dynamical equation for the prognostic equation of turbulent dissipation and specific dissipation respectively. It is found that the k–ε model better represents vertical transport of TKE than the k–l one (Trini Castelli et al., 2005). The main explanation brought by Mason (1979) and Britter et al. (1981) is that the turbulence length scale is a function of the local distance from the surface while it should be a function of the shear layer by itself, especially in the leeway region. Following this conclusion, Ying et al. (1994, 1995) concluded that the k–ε model and its equivalents (e.g. k–ω) were the least elaborated model capable of solving turbulent mean flow pattern in such cases. For these reasons we decided to use the k–ε turbulence closure scheme with modified constants to simulate the ABL. The selection of the k–ε turbulence closure scheme is done for validation purposes (common scheme in both models). More complex closure schemes (e.g. LES) could have been used but this adds an extra unknown concerning the turbulence closure scheme by itself.

The prime objective of this work is to explore the possibility of using an appropriately-modified atmospheric model (RAMS) for the description of basic flow and turbulence characteristics of the ABL at very high resolution for wind resource assessment and other wind engineering applications. In other words, RAMS solver is evaluated to reproduce local flow features due to orographic variability (detachment, recirculation). We believe that this study is a necessary (but not sufficient) condition to use RAMS at high resolution in complex terrain for wind resource assessment purpose. At this stage of work, a neutral stratification case is studied.

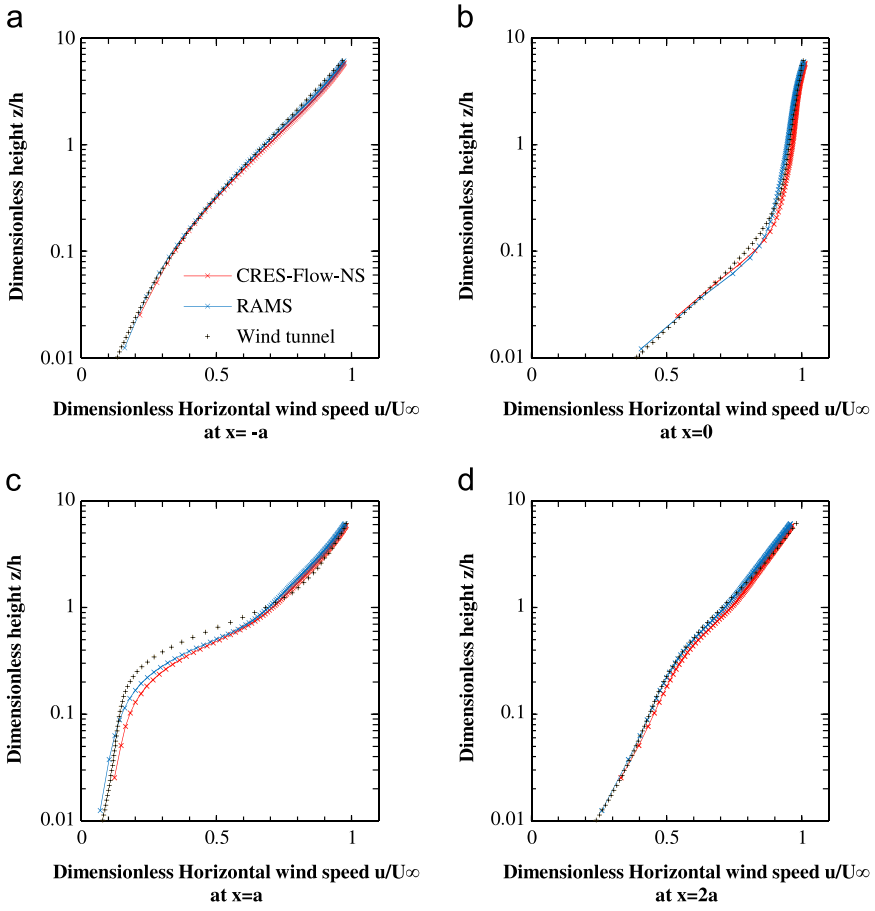

Fig. 6. Dimensionless horizontal wind speed simulated with RAMS (blue) and CRES-Flow-NS (red) at (a) $x=-a$, (b) $x=0$, (c) $x=a$, and (d) $x=2a$ for hill H5. Black crosses are wind tunnel measurements. (For interpretation of the references to color in this figure legend, the reader is referred to the web version of this article.)

To check the validity of the results, we used a state-of-the-art CFD solver and wind tunnel experimental data as references. The CFD model used is the one from Dr. P. Chaviaropoulos (Chaviaropoulos et al., 1998) of the Center for Renewable Energy Sources (CRES). The wind tunnel experimental data are taken from the US EPA (Environmental Protection Agency) RUSHIL case (Khurshudyan et al., 1981).

In the following section, we provide a general description of the models and adopted methodologies. The use of the k–ε turbulence closure scheme is then described in detail. In Section 3, the wind tunnel experimental protocol and RAMS's configuration are discussed. In Section 4, model results are discussed and each model assets and weaknesses are studied in depth with criteria relevant to wind resource assessment. Finally in Section 5 we summarize the findings and derive conclusions.

2. Models description

2.1. Mesoscale model RAMS

The RAMS model (Pielke et al., 1992; Cotton et al., 2003) uses a non-hydrostatic expression of the Ensemble Averaged Navier Stokes equations simplified to fit the characteristics of atmospheric flows (Klemp and Wilhelmson, 1978). Taking into account the compressibility of the atmosphere, the pressure is expressed in a non-dimensional form derived from the ideal gas law called Exner function:

$$\pi = c_p\left(\frac{p}{p_0}\right)^{Rd/cp} \tag{1}$$

where p denotes the pressure, p_0 its value at ground level, R_d is the gas constant for dry air, and c_p is the specific heat at constant pressure.

In their final form, after assuming that the effects of molecular viscosity are negligible, the equations are written with Einstein notations for $i=\{1,2,3\}$:

$$\frac{\partial \pi'}{\partial t} = -\frac{R_d\,\pi_0}{c_v\,\rho_0\theta_0}\frac{\partial}{\partial x_j}(\rho_0\theta_0\bar{u_j}) \tag{2}$$

$$\frac{\partial \bar{u_i}}{\partial t} = -\bar{u_j}\frac{\partial \bar{u_i}}{\partial x_j} - c_p\,\theta_0\frac{\partial \pi'}{\partial x_i} + \delta_{i3}\,g\left(\frac{\bar{\theta}}{\theta_0}-1\right) - \frac{1}{\rho_0}\frac{\partial}{\partial x_j}\left(\rho_0\,\overline{u_i'u_j'}\right) \tag{3}$$

$$\frac{\partial \bar{\theta}}{\partial t} = -\bar{u_i}\frac{\partial \bar{\theta}}{\partial x_i} - \frac{\partial}{\partial x_i}\left(K_\theta\frac{\partial \bar{\theta}}{\partial x_i}\right) \tag{4}$$

$$\frac{\partial \bar{q}}{\partial t} = -\bar{u_i}\frac{\partial \bar{q}}{\partial x_i} - \frac{\partial}{\partial x_i}\left(K_q\frac{\partial \bar{q}}{\partial x_i}\right) \tag{5}$$

$$\frac{\partial \bar{\chi_n}}{\partial t} = -\bar{u_i}\frac{\partial \bar{\chi_n}}{\partial x_i} - \frac{\partial}{\partial x_i}\left(K_\chi\frac{\partial \bar{\chi_n}}{\partial x_i}\right) \tag{6}$$

where π_0, ρ_0 and θ_0 are respectively the initial unperturbed state of Exner function, the density and potential temperature, K_θ, K_q, and K_χ are the diffusion coefficients proportional to the momentum diffusion coefficient (described in Section 2.3 below), π' is the

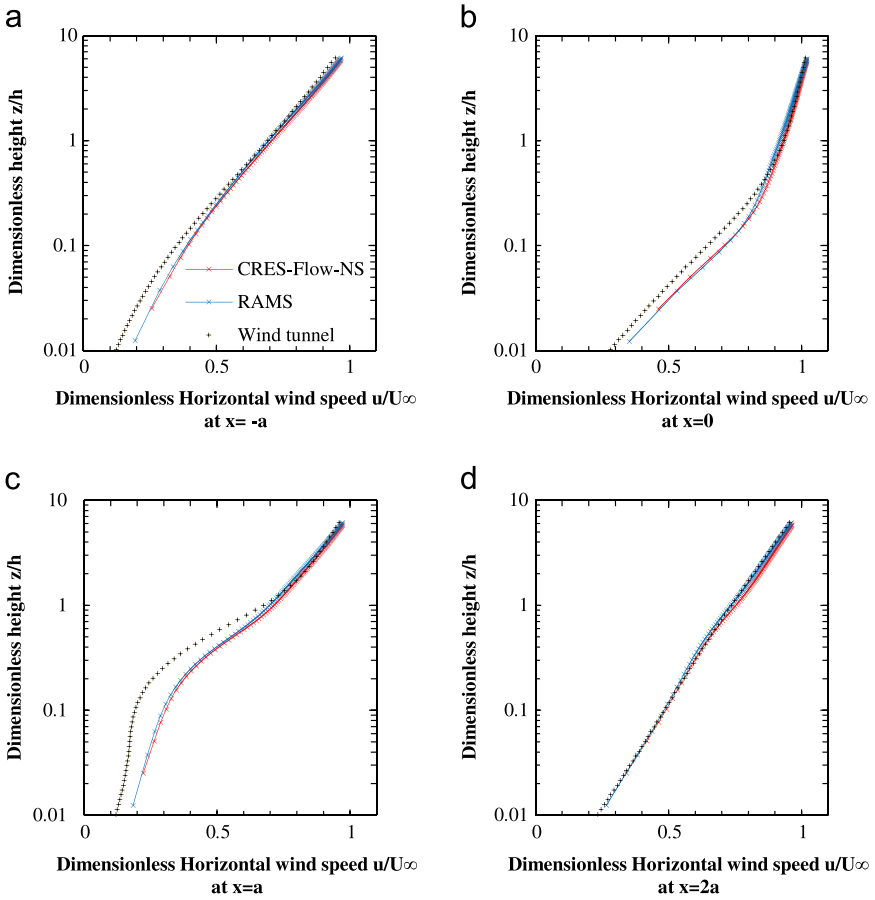

Fig. 7. Dimensionless horizontal wind speed simulated with RAMS (blue) and CRES-Flow-NS (red) at (a) $x=-a$, (b) $x=0$, (c) $x=a$, and (d) $x=2a$ for hill H8. Black crosses are wind tunnel measurements. (For interpretation of the references to color in this figure legend, the reader is referred to the web version of this article.)

deviation from π_0, c_v is the specific heat at constant volume, u_i are the wind speed components in a Cartesian coordinate system, q is the specific humidity and χ_m the mixing ratio of atmospheric gases and aerosol species considered. The over bar denotes the ensemble averaged values and the prime small fluctuations.

RAMS uses the "staggered" Arakawa C-grid discretization scheme. The RAMS model is capable of resolving a wide range of atmospheric turbulent flows according to their scale and amongst them microscale turbulent flows (Ying et al., 1994; Ying and Canuto, 1995, 1997; Trini Castelli et al., 2005, Trini Castelli and Reisin, 2010; De Wekker et al., 2005). It has several other capabilities such as the two-way interactive nesting with any number of grids and the use of a large variety of lateral Boundary Conditions (BC). It can model different levels of flow complexity.

2.2. Microscale CFD model

The CFD model used is the CRES-Flow-NS code (Chaviaropoulos and Douvikas, 1998). It solves the incompressible RANS equations for $i=\{1,2,3\}$:

$$\bar{u_j}\frac{\partial \bar{u_i}}{\partial x_j} = -\frac{1}{\rho}\frac{\partial p}{\partial x_i} - \frac{1}{\rho}\frac{\partial}{\partial x_j}\left(\rho\overline{u_i' u_j'}\right) \tag{7}$$

$$\frac{\partial \bar{u_i}}{\partial x_i} = 0 \tag{8}$$

where p is the pressure term and $\bar{u_i}\bar{u_j}$ denotes the Reynolds stress tensor.

The Reynolds stress tensor is modeled by two additional transport equations of turbulent scales (they appear as (11) and (12) in the following subsection for the k–ε turbulent closure scheme). The k–ε (Launder and Spalding, 1972), k–ω (Wilcox, 1988) and Shear Stress Transport (SST) k–ω (Menter, 1994) models are implemented. The set of equations is solved using an implicit pressure-gradient correction algorithm (Chaviaropoulos, 1998). This strategy allows a smooth coupling between momentum and pressure (the latter not being present in the mass conservation equation). The coupling is accomplished by solving a Poisson type equation for the pressure gradient.

The discretization is achieved by using a staggered grid where mean and turbulent quantities are computed at the grid points while the pressure is computed at the center of the cell removing the need for explicit pressure BC (Chaviaropoulos, 1998). Equations are solved in curvilinear body-fitted coordinates. The convective operator is discretized by the second order Total Variation Diminishing (TVD) scheme of Harten (1983). For 2D studies the Laplacian operator uses a nine-point stencil (Saad, 2003). Convergence is generally considered as obtained when the residuals of the primitive variables decrease by at least three orders of magnitude (Prospathopoulos and Voutsinas, 2006). In the context of wind resource assessment this solver has been successfully applied to several simulations over complex terrains (Prospathopoulos et al., 2010, 2012) and wind turbine wakes (Politis et al., 2012; Prospathopoulos et al., 2011).

2.3. Major difference between the two models

RAMS is used to estimate the evolution in time of the atmospheric processes provided its initial state. It is generally used for limited area weather forecasting or to analyze past events of a

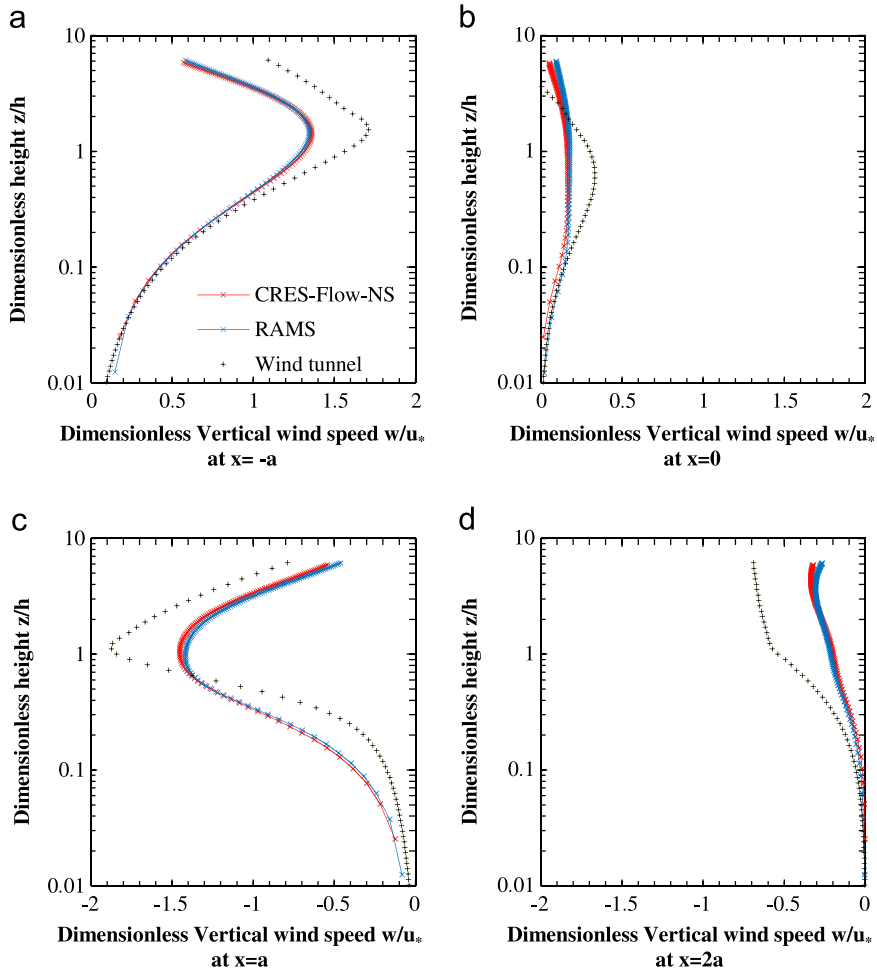

Fig. 8. Dimensionless vertical wind speed simulated with RAMS (blue) and CRES-Flow-NS (red) at (a) $x=-a$, (b) $x=0$, (c) $x=a$, and (d) $x=2a$ for hill H5. Black crosses are wind tunnel measurement. (For interpretation of the references to color in this figure legend, the reader is referred to the web version of this article.)

specific region (hindcasting). It is using Global Circulation Model (GCM) gridded fields and local observations (surface and upper-air if available) for initialization and lateral BC in order to resolve local flow features (topography or thermally driven). It is designed to solve flow features that are transient with time-scales varying from hours to less than a second.

On the other hand, the CFD model is designed to simulate steady-state neutrally-stratified flows induced by topography and surface properties. It is only aimed at resolving boundary layer processes. In this context, it is valid to assume incompressibility. These assumptions are rather similar to engineering wind flows such as flows in pipes. The code is therefore resolving incompressible steady-state Navier–Stokes equations using a pressure correction method with a finite volume approach.

The atmospheric model used in our experimental development and simulations is RAMS version 6.0. The model was modified to use the k–ε closure scheme (Trini Castelli et al., 2001) with appropriate initial and lateral boundary conditions described in Section 2.4.2. The CFD code that was used is the same as in Chaviaropoulos et al. (1998) with no other modifications except the domain configuration to be the same as in RAMS. Table 1 has been prepared summarizing the major features of each model.

2.4. The turbulence model k–ε and its use in both models

The last term of Eq. (3) for RAMS and Eq. (7) for CRES-Flow-NS can be expressed following the Boussinesq eddy viscosity assumption. In this case, the turbulent diffusion contribution is written as

$$-\frac{\partial}{\partial x_j}\left(\rho\ \overline{u_i' u_j'}\right) = \frac{\partial}{\partial x_j}\left(\mu_t\left(\frac{\partial \bar{u_i}}{\partial x_j}+\frac{\partial \bar{u_j}}{\partial x_i}\right)-\frac{2}{3}\rho k\delta_{ij}\right) \tag{9}$$

where μ_τ is the eddy viscosity, k is the TKE and δ_{ij} is the Kronecker symbol.

2.4.1. Standard k–ε turbulent closure

Using the standard k–ε turbulent closure scheme, the momentum diffusion coefficient is computed as follows:

$$\mu_t = \rho C_\mu \frac{k^2}{\varepsilon} \tag{10}$$

where C_μ is a constant, ε is the turbulent dissipation rate and ρ is the density. In RAMS, density is calculated according to Eq. (2). In the CFD model, ρ is constant following the incompressibility assumption. The dynamical equation for the TKE k and its dissipation rate ε are then written as

$$\frac{\partial(\rho k)}{\partial t}+\frac{\partial(\rho k\bar{u_i})}{\partial x_i}=\frac{\partial}{\partial x_i}\left(\frac{\mu_t}{\sigma_k}\frac{\partial k}{\partial x_i}\right)+P_s-\rho\varepsilon \tag{11}$$

$$\frac{\partial(\rho \varepsilon)}{\partial t}+\frac{\partial(\rho \varepsilon\bar{u_i})}{\partial x_i}=\frac{\partial}{\partial x_i}\left(\frac{\mu_t}{\sigma_\varepsilon}\frac{\partial \varepsilon}{\partial x_i}\right)+C_{1\varepsilon}\frac{\varepsilon}{k}P_s-C_{2\varepsilon}\rho\frac{\varepsilon^2}{k} \tag{12}$$

where σ_k, σ_ε, $C_{1\varepsilon}$, and $C_{2\varepsilon}$ are closure constants. Their values are discussed in Section 2.4.2 below. The Production term P_s is

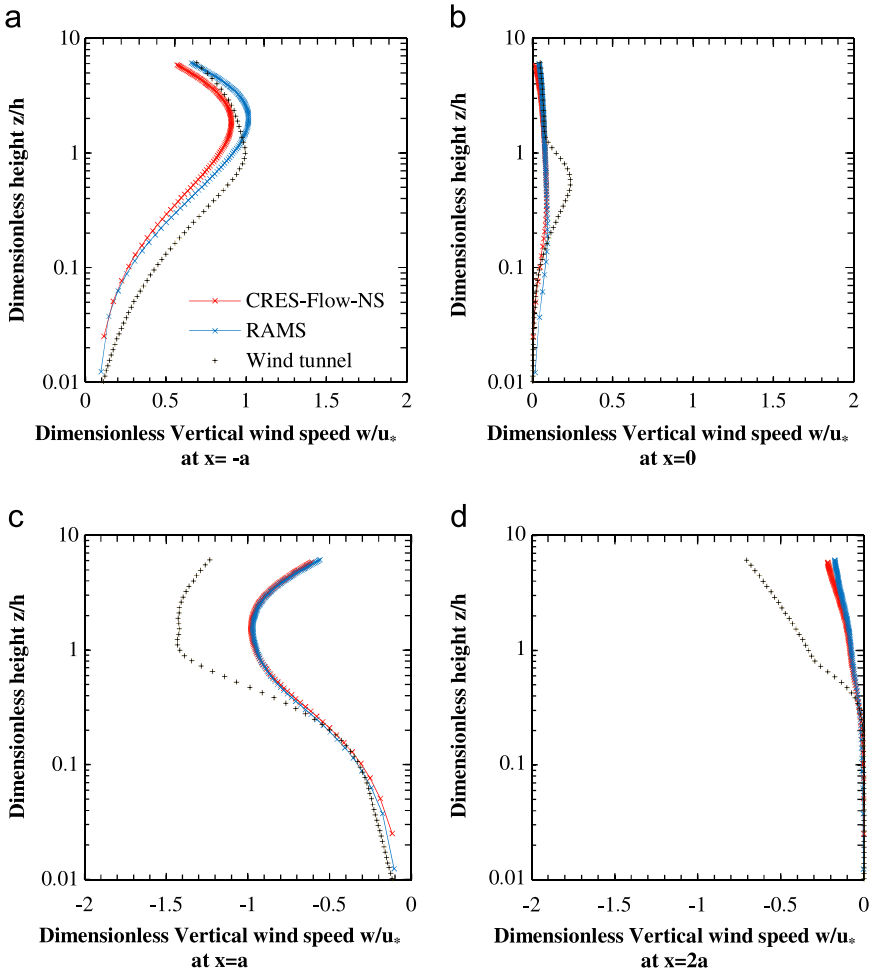

Fig. 9. Dimensionless vertical wind speed simulated with RAMS (blue) and CRES-Flow-NS (red) at (a) $x=-a$, (b) $x=0$, (c) $x=a$, and (d) $x=2a$ for hill H8. Black crosses are wind tunnel measurement. (For interpretation of the references to color in this figure legend, the reader is referred to the web version of this article.)

calculated by using the trace-less mean strain rate tensor and the diffusion coefficient:

$$P_s = 2\mu_t \left(\frac{1}{2}\left(\frac{\partial \bar{u_i}}{\partial x_j} + \frac{\partial \bar{u_j}}{\partial x_i} \right) - \frac{1}{3}\frac{\partial \bar{u_k}}{\partial x_k}\delta_{ij} \right)^2 \tag{13}$$

Since the CFD model does not take into account compressibility, the term associated with the Kronecker symbol is zero.

2.4.2. Wall functions and closure constant used in both models

In this work, we follow the generally admitted formulation of Richards and Hoxey (1993). In their work, they assume the neutral ABL as a horizontal homogenous turbulent surface layer. After deriving Eqs. (11)–(13), following the assumptions mentioned before, the expressions of the mean velocity and turbulent quantities are obtained:

$$\bar{u} = \frac{u_*}{\kappa} \ln\left(\frac{z}{z_0}\right) \tag{14}$$

$$k = \frac{u_*^2}{\sqrt{C_\mu}} \tag{15}$$

$$\varepsilon = \frac{u_*^3}{\kappa z} \tag{16}$$

Eqs. (14), (15) and (16) are used as initial, inflow and bottom BC (also called wall functions) in both models.

To properly resolve turbulent quantities, constants arising in Eqs. (11) and (12) are requiring calibration. As seen in Eq. (15), the calibration of C_μ is of great importance to obtain the expected level of TKE. The value proposed by Jones and Launder (1972) (that is generally fitting a wide range of engineering flows) results in an underestimation of the TKE when compared with measurements within the ABL. A method to correct this discrepancy is to decrease the value of C_μ (Hagen et al., 1981; Beljaars et al., 1987).

In order to maintain the local equilibrium where the production term is equal to the dissipation term in Eq. (12), Richards and Hoxey (1993) imposed a relationship between the constants:

$$\sigma_\varepsilon = \frac{\kappa^2}{(C_{2\varepsilon} - C_{1\varepsilon})\sqrt{C_\mu}} \tag{17}$$

For the present study, we used the following set of constants:

$$\{C_\mu,\ \sigma_k,\ \sigma_\varepsilon,\ C_{1\varepsilon},\ C_{2\varepsilon}\} = \{0.03,\ 1.0,\ 1.3,\ 1.22,\ 1.92\} \tag{18}$$

3. Model setup and data used

3.1. EPA RUSHIL wind tunnel experiment

The EPA RUSHIL wind tunnel experiment was designed and executed for better understanding wind flow and dispersion of pollutants over isolated 2D hills (Khurshudyan et al., 1981). The data-set produced is considered as reference for very high resolution atmospheric

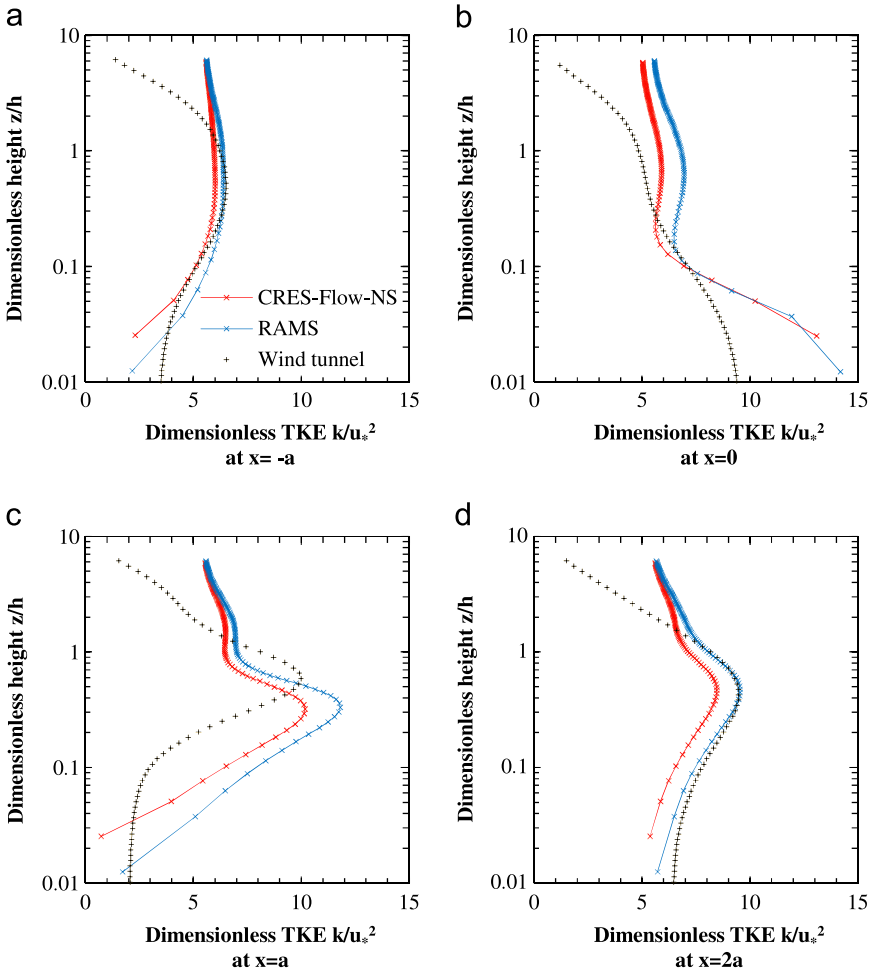

Fig. 10. Dimensionless TKE simulated with RAMS (blue) and CRES-Flow-NS (red) at (a) $x=-a$, (b) $x=0$, (c) $x=a$, and (d) $x=2a$ for hill H5. Black crosses are wind tunnel measurements. (For interpretation of the references to color in this figure legend, the reader is referred to the web version of this article.)

model evaluation. Three hills with various aspect ratios were considered in this study. Their maximum slope angle that is reached in the middle-slope section is 26%, 16% and 10% respectively and denoted as H3, H5 and H8. The schematic representation of these hills and the horizontal wind inflow profile are illustrated in Fig. 1.

The wind tunnel inflow is set up to reproduce a neutrally stratified ABL of 600 m. The scaling was set such as 1 m in the wind tunnel represents 600 m at ABL scale. The dimensions of the test section area are 3.7 m wide, 2.1 m high and 18.3 m long. The hill coordinates are given from the parametric equations:

$$\forall\ |\xi| \le a \begin{cases} x(\xi) = \frac{1}{2}\xi\left[1 + \frac{a^2}{\xi^2 + m^2\left(a^2 - \xi^2\right)}\right] \\ z(\xi) = \frac{1}{2}m\sqrt{a^2 - \xi^2}\left[1 - \frac{a^2}{\xi^2 + m^2\left(a^2 - \xi^2\right)}\right] \end{cases}$$

$$\text{with } m = \frac{h}{a} + \sqrt{\left(\frac{h}{a}\right)^2 + 1} \qquad (19)$$

where z is the height given at a location x in the horizontal direction, h is the hill height and a is the semi-length of the hill. The ratio a/h for the three hills is 3, 5 and 8 going from the steepest to the flattest hill. The hill-height is maintained constant to 11.7 cm for all tests.

The experiment provides data of mean flow fields such as wind speed and turbulent shear stress in 15 vertical cross-sections placed upwind, at the top and the leeway. The locations along the horizontal axis where measurements are made are illustrated in Fig. 2.

3.2. RAMS model setup and configuration

The RAMS model requires some simplifications and modifications to make the comparison with CFD as close and as fair as possible. More specifically, the specific humidity parameter is maintained to zero following the experimental protocol of EPA RUSHIL experiment. Short and long wave radiation schemes are "switched off" to avoid any convection occurring that would trigger the formation of an unstable ABL. Therefore, the potential temperature gradient is maintained to zero throughout the entire domain and along the integration time. In addition, the surface processes (soil temperature and moisture sub-model) have been "switched off". Several grid configurations are studied (detailed in Section 4.1) and the final domain is composed of 1800 grid points in the horizontal direction and 310 in the vertical direction. The vertical grid increment is kept constant at the value of 1.01.

The RAMS model is designed to resolve dynamical and thermodynamical atmospheric processes at a wide range of scales. It is commonly used on hindcasting or forecasting mode and is not aimed at solving steady-state flow conditions. However, in order to evaluate the model in reproducing steady-state flow conditions, a careful setup of initial and boundary (inflow and bottom) conditions is required. With respect to the turbulence closure scheme used, the inlet Dirichlet BC and the initial 2D field is set to follow equations from Eqs. (14) to (16). A second-type Neumann BC is

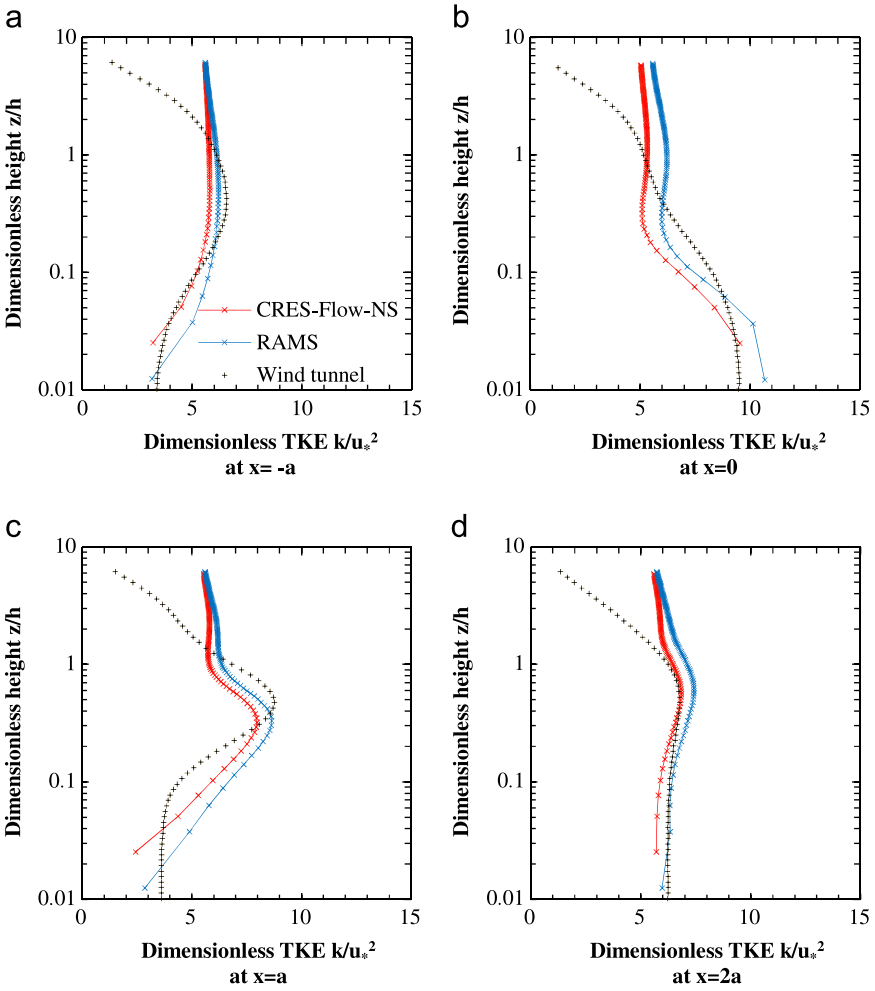

Fig. 11. Dimensionless TKE simulated with RAMS (blue) and CRES-Flow-NS (red) at (a) $x=-a$, (b) $x=0$, (c) $x=a$, and (d) $x=2a$ for hill H8. Black crosses are wind tunnel measurements. (For interpretation of the references to color in this figure legend, the reader is referred to the web version of this article.)

used at the outlet to avoid the reflection of propagating waves through the model domain (Pielke et al., 1992).

Within the wind tunnel, the horizontal mean wind speed follows a logarithmic law profile with a constant roughness length z_0 equal to 0.2 mm. The friction velocity is deduced from the constant horizontal wind speed of 3.9 m/s (denoted $U_{\infty)}$ obtained at the ABL top z_{ABLtop} that is 1 m in the wind tunnel:

$$u_* = \frac{U_\infty \kappa}{\ln\left(\frac{z_{ABL\ top}}{z_0}\right)} \tag{20}$$

The two numerical models (RAMS and CRES-Flow-NS) used in this evaluation are set up to reproduce the wind tunnel experimental conditions by running them at the actual atmospheric scale. This is achieved by multiplying each length quantity described in the wind tunnel (e.g. hill dimensions, ABL top, roughness length) by 600. The wind speed logarithmic profile is not modified. In fact, as seen in Eq. (20), the value of the friction velocity u_* remains identical since each member in the fraction (e.g. z_{ABLtop} and z_0) are both multiplied by 600. The model was calibrated according to the generally-admitted atmospheric constants listed in Eq. (18).

In this configuration, the Reynolds number similarity assumption is not completed. However, the flow can be assumed as Reynolds number independent because of the following conditions: (1) the flow is considered as fully turbulent with no stratification and Coriolis; (2) the minimum Reynolds number is above a threshold value that is defined by Snyder (1981) as 10,000. This is the case for the wind tunnel configuration (US EPA RUSHIL) used for comparison.

3.3. RAMS model convergence conditions

The model is run through a certain period of time until the prognostic quantities, such as wind speed, converge to a time independent value. Fig. 3 shows the convergence of wind speed components, TKE and TKE dissipation rate at 20 m height at several locations for hill H3. To a certain extent, all these variables reach a constant trend after running the RAMS model for approximately one hour from cold start initialization.

During the first time steps, the model is quickly adjusting wind speed to the local pressure deficit observed in the leeside. At hill top, the speed-up is overestimated as compared with its final value. In the near-wake the velocity deficit is underestimated (Fig. 3a). On the other hand, scalars such as TKE and TKE dissipation rate (Fig. 3c and d) are adjusting very slowly. After a few iterations, the velocity components are slowly converging towards a solution constant in time. Downhill, at $x=a$, the TKE and the TKE dissipation rates reach a maximum after 120 s and are then slowly decreasing towards respective values of 0.6 m^2/s^2 and 0.004 m^2/s^3, as illustrated in Fig. 3c and d.

We consider as a good indicator of convergence the fact that the wind speed components reach a steady value after a certain number of time steps (Fig. 3a and b). For scalars, the solution in the

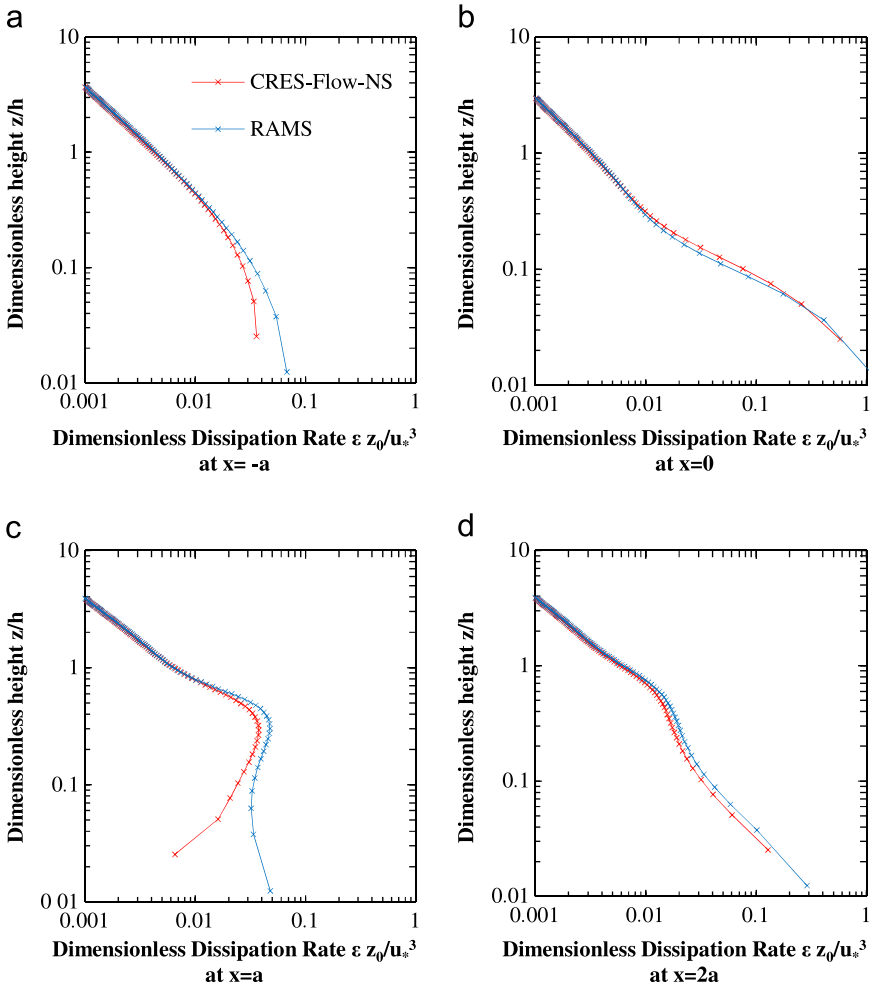

Fig. 12. Dimensionless turbulent dissipation rate simulated with RAMS (blue) and CRES-Flow-NS (red) at (a) $x=-a$, (b) $x=0$, (c) $x=a$, and (d) $x=2a$ for hill H5. (For interpretation of the references to color in this figure legend, the reader is referred to the web version of this article.)

leeside shows a relatively small oscillation. This can be attributed to slightly unsteady recirculation (Fig. 3c and d). From a mathematical point of view, it is difficult to state that convergence is strictly obtained. In fact and as stated by Trini Castelli et al. (2005), the model is not aimed at resolving steady state flows and is generally resolving transient phenomena that are observed in the atmosphere. Nevertheless, the global solution obtained after running RAMS for one hour can be considered as steady.

4. Results and discussion

4.1. Grid independency and intrinsic comparison

An important issue concerning both model simulations (RAMS and CRES-Flow-NS) is the grid refinement (both in the vertical and horizontal). In this section, a method is proposed to quantitatively assess the proper grid refinement for both models (in both x and z directions) necessary to resolve the mean wind speed-up and recirculation pattern for the hill H3 case.

Fig. 4 demonstrates the importance of mesh refinement in the vertical direction to accurately resolve mean wind speed profiles. As it is seen in this figure, RAMS requires a higher vertical resolution to attain grid independency at hill top as compared with the CFD model. In the recirculation zone (Fig. 4c and d), the same resolution is required in the region of strong shear at $z/h=0.3$. Since the CFD model is capable of using finer vertical grid spacing near the ground as compared with the RAMS model, additional runs were made with a vertical resolution of 1 m and 0.5 m. The results were slightly improved in the recirculation region. However we retained the vertical grid spacing of 1.755 m as the finer grid configuration for model evaluation/intercomparison purpose.

The influence of horizontal mesh refinement is presented in Fig. 5 for the case of hill H3 (that has a length of 420 m and a height of 70.2 m). The results of the two models have been examined in three cases with different horizontal grid discretization: coarse ($\Delta x=14$ m), relatively fine ($\Delta x=7$ m) and fine ($\Delta x=3.5$ m). In other words, the hill length is discretized by using 30, 60 and 120 grid points.

At hill top (Fig. 5a and b), it was found that RAMS required a higher resolution than the CFD model to obtain a grid independent solution. The results obtained with RAMS coarse resolution simulations presented an underprediction of the wind flow profile above the dimensionless height of 0.1. On the other hand, the CFD model obtained a grid independent solution for all grid configurations used. However, this model overpredicted the wind flow profile as compared with the RAMS model. The latter one showed very good agreement with the experimental data with a relatively fine horizontal grid spacing.

In the recirculation region (Fig. 5c and d), both models easily obtained a mesh independent solution with the coarse grid configuration. As a general remark, we can say that RAMS better represented the recirculation as compared with the CFD model used with the fine grid configuration.

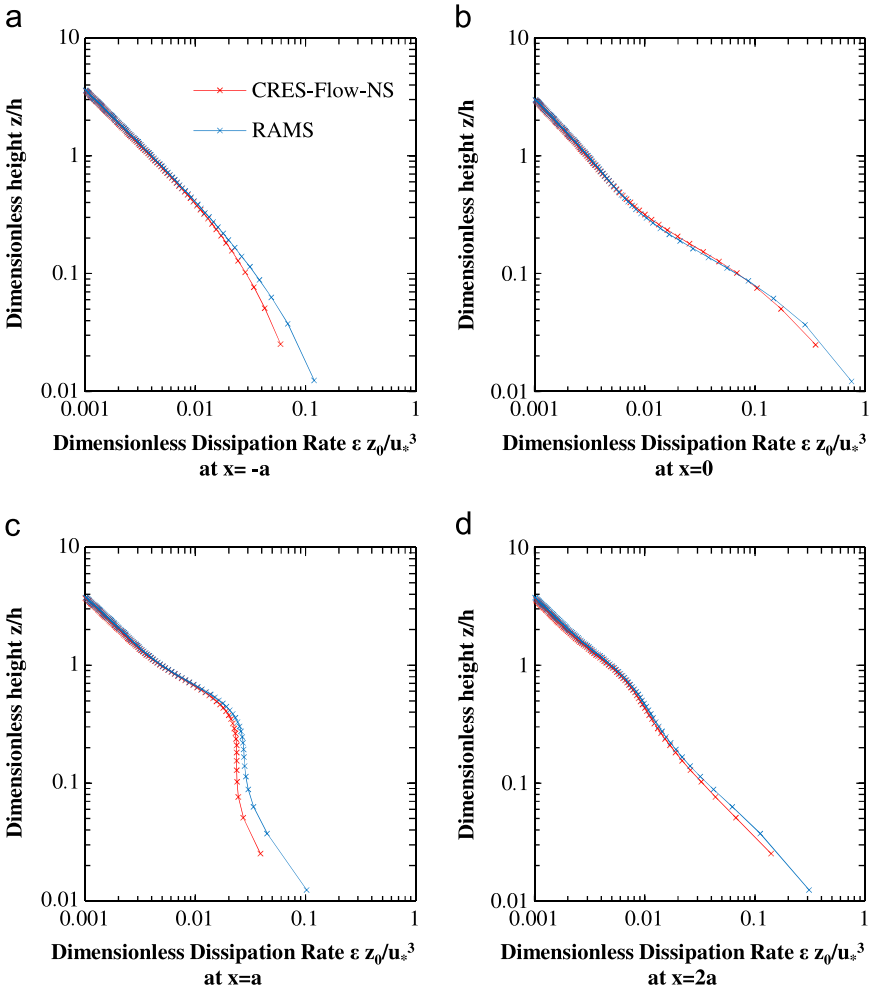

Fig. 13. Dimensionless turbulent dissipation rate simulated with RAMS (blue) and CRES-Flow-NS (red) at (a) $x=-a$, (b) $x=0$, (c) $x=a$, and (d) $x=2a$ for hill H8. (For interpretation of the references to color in this figure legend, the reader is referred to the web version of this article.)

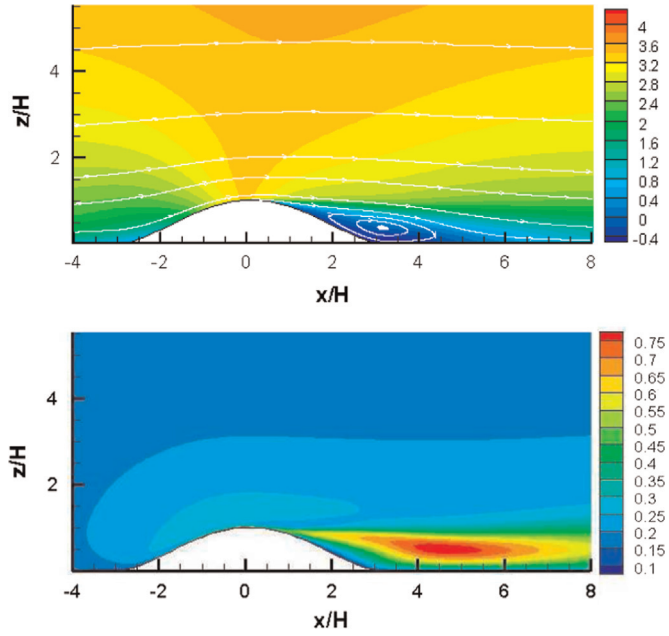

Fig. 14. 2D cross-section of horizontal wind speed (color palette) and streamlines (top) and TKE (bottom) as simulated with RAMS. (For interpretation of the references to color in this figure legend, the reader is referred to the web version of this article.)

4.2. Fine mesh comparison between CFD and MM

In this section, the detailed analysis of both model results is discussed with respect to the EPA RUSHIL data set. The fine mesh model configuration was selected. The model-wind tunnel intercomparison is performed with respect to the mean flow pattern characteristics. Hill H5 and H8 are of gentle slope and therefore the flow does not exhibit significant non-linear features. The hill denoted as H3 is intended to generate recirculation.

4.2.1. Gentle hill slopes: hills H5 and H8

The study of hills H5 and H8 are discussed together since they do not have reverse flow and the results are relatively similar. In order to avoid redundant comments, we will discuss results from hill H5 in detail and we will refer to differences with hill H8 when necessary.

In the case of average steep slopes (hill H5), the horizontal wind speed profile was accurately captured by both models. At $x=2a$, it is very similar to the inflow profile as illustrated in Fig. 6. In the downslope region, in the inner layer[1], the wind flow is highly-influenced by the hill but the pressure gradient is not strong enough to produce significant detachment. The best

[1] The terminology of the outer and inner layers is expressed following the definition given by Jackson and Hunt (1975). The dimensionless height delimiting the two regions is 0.126 for H3, 0.192 for H5 and 0.246 for H8.

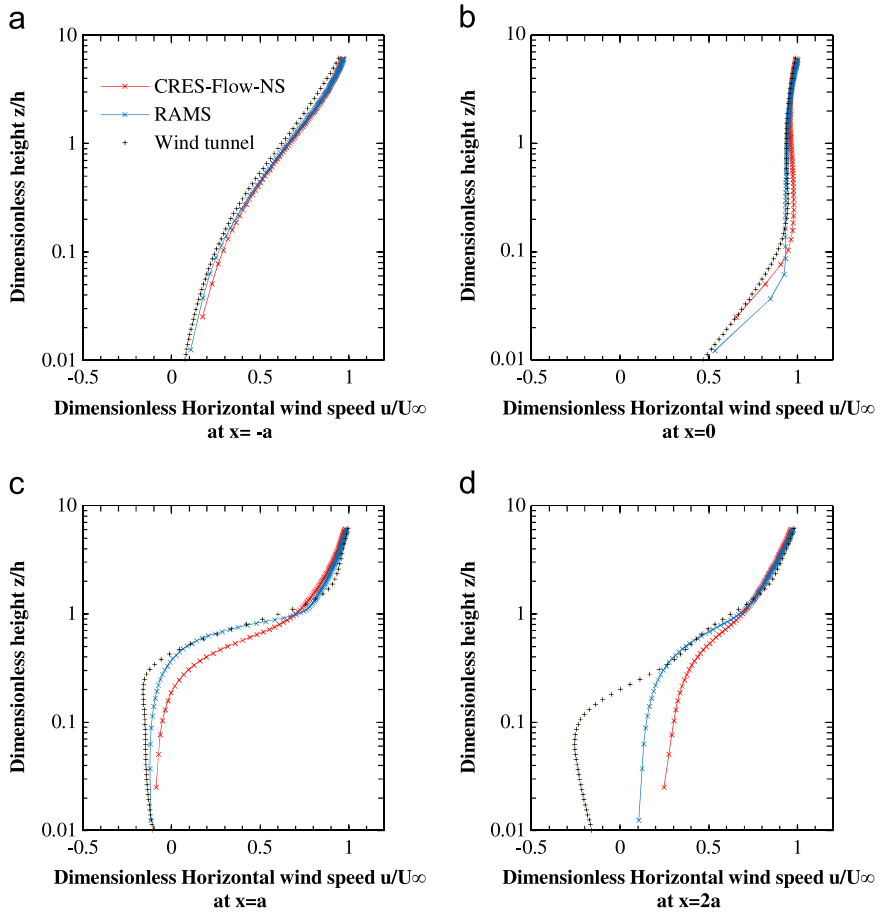

Fig. 15. Dimensionless horizontal wind speed simulated with RAMS (blue) and CRES-Flow-NS (red) at (a) $x=-a$, (b) $x=0$, (c) $x=a$, and (d) $x=2a$ for hill H3. Black crosses are wind tunnel measurements. (For interpretation of the references to color in this figure legend, the reader is referred to the web version of this article.)

agreement between the two models and the wind tunnel measurements was achieved for the case of hill H5.

Similar results were found for hill H8 concerning the horizontal wind speed. However, a deviation from the observations was found in some of the considered profiles. From the inflow to the top of the hill, the horizontal wind speed was overestimated near the ground and up to about a dimensionless height of 0.3 by both models (Fig. 7a and b). At the near-wake region, the overestimation was extended up to about a dimensionless height of 1 (Fig. 7c). Both models compared well with the wind tunnel data at the near outflow region ($x=2a$) as illustrated in Fig. 7d.

For the case of hill H5, the vertical velocity estimated by both models is similar as shown in Fig. 8 but both of them deviate significantly from the wind tunnel measurements. More specifically, both models underestimate vertical velocity at the outer layer of the inlet region (see Fig. 8a and b). The opposite is observed in the outer layer at $x=a$ and $x=2a$ as shown in Fig. 8c and d. These deviations can be at least partially due to the low levels of TKE observed in the wind tunnel in the outer layer. In general, the k–ε turbulence closure scheme is less accurate in low turbulent flows than in highly turbulent ones (Wilcox, 1988). In the inner layer, the models and experimental data are in general in better agreement everywhere except at the near-wake region where both models underestimate the vertical velocity (Fig. 8c).

In general, for hill H8, we observe a similar behavior as seen in hill H5 by both models. Although, a better fitting to measurements is observed at $x=-a$ and $x=a$ as shown in Fig. 9.

As seen in Fig. 10, both models computed similar TKE vertical profiles in general. The CFD model tends to compute lower values in all profiles as compared with RAMS. At hill top both models significantly overestimated the TKE in the first grid points above the ground level (see Fig. 10b). This is probably due to the TKE parameterization in the first grid cell near the ground. In the near-wake of the hill, at $x=a$, the maximum value of TKE occurs at a different height in the wind tunnel as compared with the two models (see Fig. 10c). A probable cause of this deviation of models results from the wind tunnel measurements should be attributed to the advection schemes used in both models. At the outer region, the models always overestimate the TKE as compared with the experimental data-set. There is no clear explanation for these differences.

Measurements to model comparison for hill H8 shows a better agreement as illustrated in Fig. 11. Particularly, the peak of TKE obtained at $x=a$ in the near-wake region is well captured by both models (intensity and height) contrary to the hill H5 case (see Fig. 10c). The problem with the overestimation of TKE at hill top has been significantly diminished in the case of hill H8 as illustrated in Fig. 11b.

Results of the TKE dissipation rate are not available from the experiments. However, comparing CRES-Flow-NS and RAMS, the two models match well with regard to the computation of the TKE dissipation rate. This can be considered as an indication of a proper implementation of the dynamical equation for TKE dissipation rate. The TKE dissipation rate profiles match very well except in the near-wall region for profiles at $x=-a$ and mostly at $x=a$ (see Fig. 12a and c). In these cases, the RAMS model clearly estimated larger values for TKE dissipation rates on the first grid points near the ground. A careful investigation of the TKE dissipation rate dynamical equation and its parameterization at the first grid cell above the ground level (a.g.l) was performed for both models. It was found that the computation of scalars within RAMS is done at the cell

center while for CFD it is done at the cell top. The parameterization of the first grid point (see Eq. (16)) is linearly dependent to the inverse of the height a.g.l. Since both models use the same parameterization but take different reference heights, their values can significantly deviate from one model to the other. The deviation is not observed at $x=0$ and $x=2a$ probably because the assumptions taken to compute the wall functions (flat terrain, horizontal homogeneous flow) are probably much more accurate in such locations.

In the case of hill H8, a better correlation is found between the two models as shown in Fig. 13.

4.2.2. Steep orography: hill H3

Hill H3 is the steepest case and therefore the most challenging to accurately simulate the flow characteristics. In fact, the steepness of the hill is enhancing recirculation in the leeway that is physically unsteady. This is illustrated in Fig. 14. RAMS is also known to face difficulties in computing gradients where cells are highly skewed due to a limitation in the metrics. RAMS uses a terrain following coordinate system and, to compute gradients accurately, the horizontal grid size must be fine enough as compared with the vertical grid size (Mahrer, 1984). Technically speaking, the aspect ratio $\Delta z/\Delta x$ must be of the order of one to a tenth ($\sim 1/10$). Still, RAMS is capable of resolving mean wind flow pattern with a linear eddy viscosity model accurately. However RAMS remains less accurate when the flow is detaching and recirculating (see Fig. 15c and d as compared with Fig. 6c and d). Similar trend is also seen in the CFD model.

The horizontal wind flow pattern in the outer layer has been satisfactorily computed above the dimensionless height of 1 as compared with the experimental data (Fig. 15). The inflow is well described by the two models along the entire profile (Fig. 15a).

At hill top, RAMS and CFD (to a smaller extent) models are slightly overpredicting the speed-up factor in the inner layer as illustrated in Fig. 15b. This trend has already been observed by Apsley and Castro (1997). According to their opinion, the error can be attributed to the methodology followed during the wind tunnel experiment. In fact, the inner layer is facing high turbulence intensity. Hot-wire instruments used in the experiment are known to be less accurate in such conditions.

In the recirculation region, at $x=a$ and $x=2a$, the measurements showed a stronger recirculation pattern as compared with both models. This is especially true at $x=2a$ (Fig. 15d) where the measurements are displaying negative values under the dimensionless height of 0.1 while both models present small positive ones. This is a well-known problem of the k–ϵ turbulent closure scheme also encountered in engineering studies.

The vertical wind speed is accurately captured in the upwind and in the near-wake region. The maximum absolute value is located at the same height for both models and in the wind tunnel experiment as shown in Fig. 16a, c and d. At hill top, the two models underestimated the predicted vertical wind speed (Fig. 16b). At this location, the experimental data include a strong positive vertical component near the ground. This seems to be unrealistic because of the neighboring with the ground where the vertical wind speed must be close to zero. Similar concerns have been expressed in Ying et al. (1994).

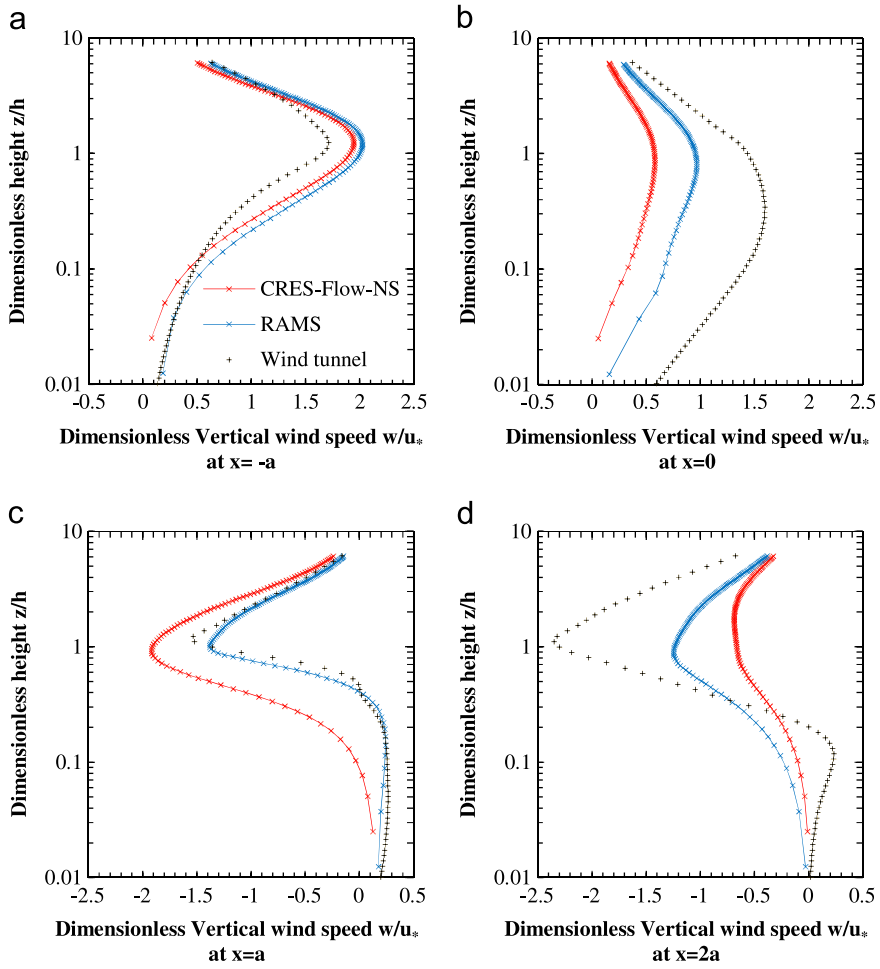

Fig. 16. Dimensionless vertical wind speed simulated with RAMS (blue) and CRES-Flow-NS (red) at (a) $x=-a$, (b) $x=0$, (c) $x=a$, and (d) $x=2a$ for hill H3. Black crosses are wind tunnel measurements. (For interpretation of the references to color in this figure legend, the reader is referred to the web version of this article.)

In both models, TKE is overpredicted as compared with the experimental data. As shown in Fig. 17, the asymptotical part of both CFD and RAMS results are highly correlated. In the near wall region, a systematic error is encountered along the horizontal axis. This can be attributed to the parameterization of the TKE near the bottom BC expressed in Eq. (15) where horizontally homogenous flow is assumed. This is not necessary the case in detached flows. The behavior of each model in regard of this limitation may lead to different and deviated results.

For the TKE dissipation rate, the two models showed deviations between them in the near wall region as illustrated in Fig. 18. In the wake region, RAMS showed higher values as compared with the CFD model. This reveals again the different behavior of both models in unsteady regions where the flow is recirculating. It is highly possible that the k–ε model is deficient in such conditions and that a more complex turbulent closure scheme is required to obtain accurate information of turbulence characteristics.

5. Conclusions

The results of a state-of-the-art atmospheric model (RAMS) were compared with an incompressible CFD solver (CRES-Flow-NS) and wind tunnel experimental data (US EPA RUSHIL). The comparison was realized for two-dimensional unstratified flow forcing over single-bell shaped hills with various steepness.

Under forced Dirichlet inlet BC, the RAMS model converged towards a quasi-steady state solution. Using meshes of diverse refinements, we obtained a grid independent solution. The grid independency was reached by the CFD model with a lower resolution. Using similar grid configuration, turbulence closure and BC, we focused on the quality of the flow solver by itself.

The major differences between the two models are related to the TKE dissipation rate at the downslope region, near the ground. We attributed this source of error to the way it has been computed at the first grid node. The horizontal wind speed is better captured by the RAMS model in the recirculation region of the steep hill case. This shows its capability to better resolve the mean wind speed pattern in regions where the flow is highly transient. In many cases both models were converging towards a similar solution that was deviating from the wind tunnel data. This shows some limitations of the k–ε approach. In some cases, there is not a clear trend showing that one model is outperforming the other. In the case of the steep hill, at its top, the speed-up ratio was better captured near the wall by the CFD model while the asymptotic value was better reproduced by RAMS. In general, the improved version of RAMS managed to achieve a proper description of the neutrally-stratified flow.

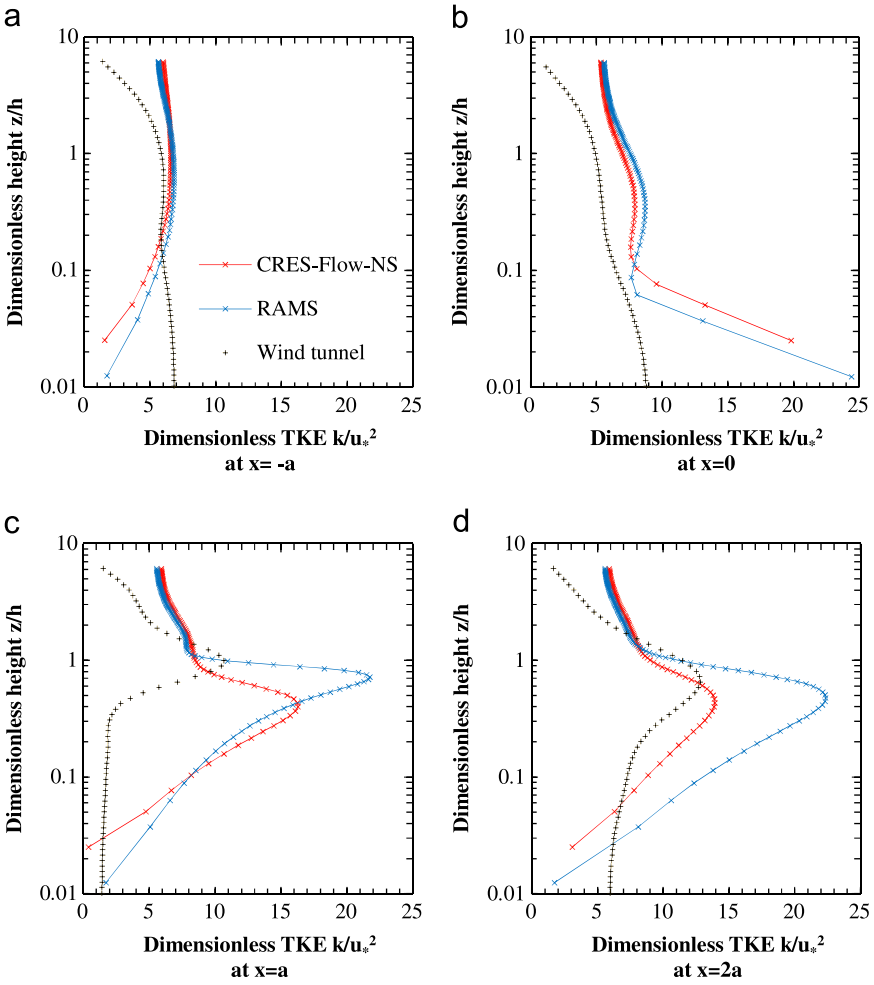

Fig. 17. Dimensionless TKE simulated with RAMS (blue) and CRES-Flow-NS (red) models at (a) $x=-a$, (b) $x=0$, (c) $x=a$, and (d) $x=2a$ for hill H3. Black crosses are wind tunnel measurements. (For interpretation of the references to color in this figure legend, the reader is referred to the web version of this article.)

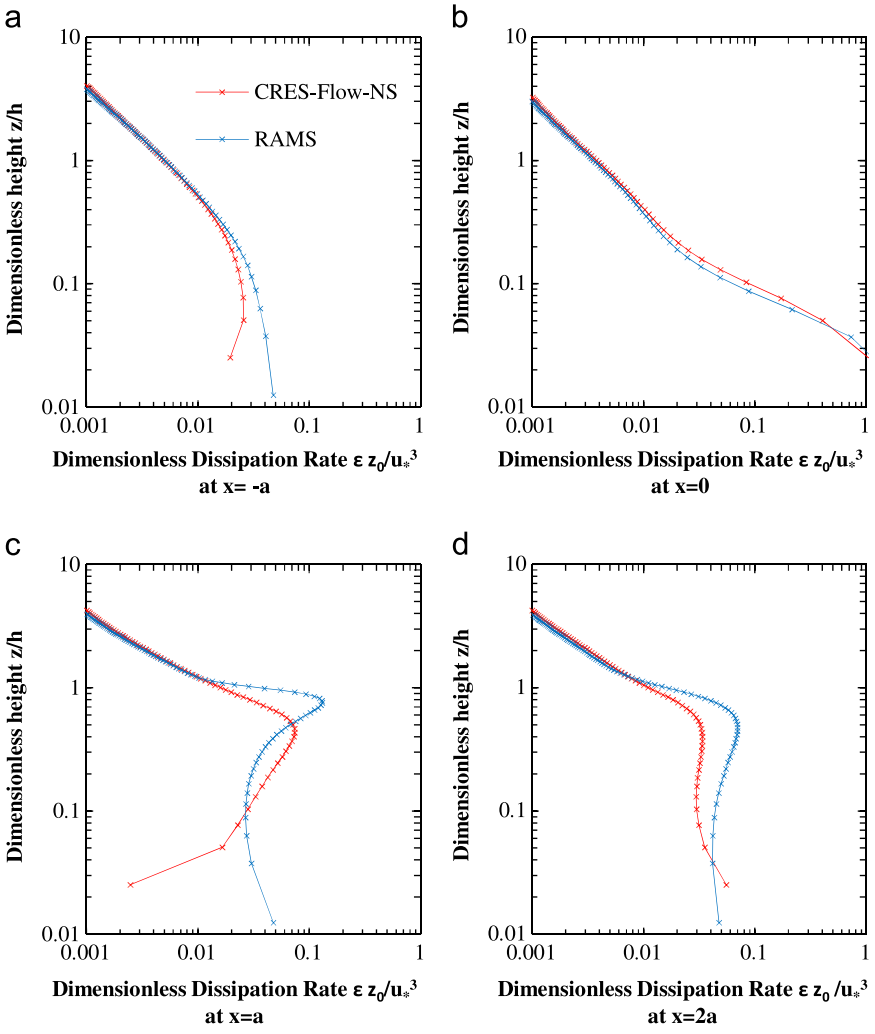

Fig. 18. Dimensionless turbulent dissipation rate simulated with RAMS (blue) and CRES-Flow-NS (red) models at (a) $x=-a$, (b) $x=0$, (c) $x=a$, and (d) $x=2a$ for hill H3. (For interpretation of the references to color in this figure legend, the reader is referred to the web version of this article.)

One thing that is clearly defined is that the atmospheric model RAMS behaves at least as good as a well-known CFD model (with similar grid configuration) in the case of an unstratified flow forcing over a single bell-shaped hill. However, the CFD model does not require a grid structure as fine as RAMS to obtain comparable mean wind speed profiles. This advantage is probably accentuated when dealing with terrain of higher complexity.

This leaves the field open to continue development by incorporating stratification. Using an atmospheric model for resolving microscale flow features is becoming more and more realistic for wind engineering applications. In addition to the above, atmospheric models with other capabilities such as the two-way nesting make them even more attractive. On the other hand, CFD models are now incorporating atmospheric features such as stability and Coriolis forcing with techniques of various complexity. Of course a next step could be towards the evaluation of the models in the case of a stratified flow forcing over complex terrain.

Acknowledgments

The authors would like to thank Dr. Silvia Trini Castelli for her availability in explaining RAMS previous work intended with microscale flows, Dr. Panagiotis Chaviaropoulos from CRES for his precious advices concerning CFD modeling and Christos Statho-poulos for his suggestions on improving the quality of the manuscript. Finally, we would like to thank the anonymous reviewers who contributed significantly on improving the quality of the paper. This work was supported by the Marie Curie Initial Training Network Project WAUDIT, Ref. #238576 and by the Integrated Research Programme on Wind Energy (IRPWIND), Ref. #609795.

References

Apsley, D.D., Castro, I.P., 1997. Flow and dispersion over hills: comparison between numerical prediction and experimental data. J. Wind Eng. Ind. Aerodyn. 67–68, 375–386.

Beaucage, P., Brower, M.C., Tensen, J., 2011. Evaluation of four numerical wind flow models for wind resource mapping. In: Proceedings of the AWEA WINDPOWER.

Beljaars, A.C.M., Walmesley, J.L., Taylor, P.A., 1987. A mixed spectral finite-difference model for neutrally stratified boundary-layer flow over roughness changes and topography. Bound.-Layer Meteorol. 38 (3), 273–303.

Blakadar, A.K., 1962. The vertical distribution of wind and turbulent exchange in the neutral atmosphere. J. Geophys. Res. 67 (8), 3095–3102.

Britter, R.E., Hunt, J.C.R., Richards, K.J., 1981. Air flow over a two-dimensional hill: studies of velocity speed-up, roughness effects and turbulence. Q. J. R. Meteorol. Soc. 107 (451), 91–110.

Chaviaropoulos, P.K., Douvikas, D.I., 1998. Mean flow field simulations over complex terrain using a 3D Reynolds Average Navier Stokes solver. In: Proceedings of the 98 Conference ECCOMAS. Athens.

Chen, K., Song, M.X., Zhang, X., 2013. A statistical method to merge wind cases for wind power assessment of wind farm. J. Wind Eng. Ind. Aerodyn. 119, 69–77.
Chow, F.K., Street, R.L., 2009. Evaluation of turbulence closure models for large-eddy simulation over complex terrain: flow over Askervein Hill. J. Appl. Meteorol. Climatol. 48 (5), 1050–1065.
Cotton, W.R., Pielke Sr., R.A., Walko, R.L., Liston, G.E., Tremback, C.J., Jiang, H., McAnelly, R.L., Harrington, J.Y., Nicholls, M.E., Carrio, G.G., Mc Fadden, J.P., 2003. RAMS 2001: current status and future directions. Meteorol. Atmos. Phys. 82, 5–29.
Deardorff, J., 1980. Stratocumulus-capped mixed layers derived from a three dimensional model. Bound. -Layer Meteorol. 18 (4), 495–527.
De Wekker, S.F.J., Steyn, D.G., Fast, J.D., Rotach, M.W., Zhong, S., 2005. The performance of RAMS in representing the convective boundary layer structure in a very steep valley. Environ. Fluid Mech. 5 (1–2), 35–62.
Galanis, G., Louka, P., Katsafados, P., Kallos, G., Pytharoulis, I., 2006. Application of Kalman filters based on non-linear functions to numerical weather predictions. Ann. Geophys. 24 (10), 2451–2460.
Gopalan, H., Gundling, C., Brown, K., Roget, B., Sitaraman, J., Mirocha, J.D., Miller, W.O., 2014. A coupled mesoscale–microscale framework for wind resource estimation and farm aerodynamics. J. Wind Eng. Ind. Aerodyn. 134, 13–26.
Hagen, L.J., Skidmore, E.L., Miller, P.L., Kipp, J.E., 1981. Simulation of the effect of wind barriers on airflow. Trans. ASAE 24, 1002–1008.
Harten, A., 1983. High resolution schemes for hyperbolic conservation laws. J. Comp. Phys. 49 (3), 357–393.
Jackson, P.S., Hunt, J.C.R., 1975. Turbulent wind flow over a low hill. Q. J. R. Meteorol. Soc. 101, 929–955.
Joensen, A., Giebel, G., Landberg, L., Madsen, H., Nielsen, H, 1999. Model output statistics applied to wind power prediction. In: EWEC Proceedings. Nice, France, pp. 1177–1180.
Jones, W.P., Launder, B.E., 1972. The prediction of laminarization with a two-equation model of turbulence. Int. J. Heat Mass Transf. 15 (2), 301–314.
Kalnay, E., 2002. Atmospheric Modeling, Data Assimilation and Predictability. Cambridge University Press, Cambridge, UK.
Khurshudyan, L.H., Snyder, W.H., Nekrasov, I.V., 1981. Flow and Dispersion of Pollutant Over Two Dimensional Hills. US EPA Report EPA/4-81-067.
Klemp, J.B., Wilhelmson, R.B., 1978. The simulation of three-dimensional convective storms dynamics. J. Atmos. Sci. 35 (6), 1070–1096.
Landberg, L., 1994. Short-Term Predictions of Local Wind Conditions (Ph.D. thesis). Riso.
Launder, B.E., Spalding, D.B., 1972. Mathematical Models of Turbulence. Academic Press, London, UK and New York, US.
Louka, P., Galanis, G., Siebert, N., Kariniotakis, G., Katsafados, P., Kallos, G., Pytharoulis, I., 2008. Improvements in wind speed forecasts for wind power prediction purposes using Kalman filtering. J. Wind Eng. Ind. Aerodyn. 96 (12), 2348–2362.
Lundquist, K.A., Chow, F.K., Lundquist, J.K., 2012. An immersed boundary method enabling large-eddy simulations of complex terrain in the WRF model. Mon. Weather Rev. 140 (12), 3936–3955.
Mahrer, Y., 1984. An improved numerical approximation of the horizontal gradients in a terrain-following coordinates system. Mon. Weather Rev. 112 (5), 918–922.
Marjanovic, N., Wharton, S., Chow, F.K., 2014. Investigation of model parameters for high-resolution wind energy forecasting: case studies over simple and complex terrain. J. Wind Eng. Ind. Aerodyn. 134, 10–24.
Mason, P.J., Sykes, R.I., 1979. Flow over isolated hills of moderate slopes. Q. J. R. Meteorol. Soc. 105 (444), 383–395.
Mellor, G.L., Yamada, T., 1982. Development of a turbulent closure model for geophysical fluid problems. Rev. Geophys. Space Phys. 20 (4), 851–875.
Menter, F.R., 1994. Two-equation eddy viscosity turbulence models for engineering applications. AIAA J. 32, 1598–1605.
Michalakes, J., Dudhia, J., Gill, D., Henderson, T., Klemp, J., Skamarock, W., Wang, W., 2004. The weather reseach and forecast model: software architecture and performance. In: George Mozdzynski (Ed.), Proceedings of the 11th ECMWF Workshop on the Use of High Performance Computing in Meteorology. Reading, UK.
Mirocha, J.D., Lundquist, J.K., Kosovic., B., 2010. Implementation of nonlinear subfilter turbulence stress models for large-eddy simulations in the advanced research WRF model. Mon. Weather Rev. 138 (11), 4212–4228.
Patankar, S.V., Spalding, D.B., 1972. A calculation procedure for heat, mass and momentum transfer in three dimensional parabolic flows. Int. J. Heat Mass Transf. 75 (10), 1787–1806.
Pielke, R.A., Cotton, W.R., Walko, R.L., Tremback, C.J., Lyons, W.A., Grasso, L.D., Nicholls, M.E., Moran, M.D., Wesley, D.A., Lee, T.J., Copeland, J.H., 1992. A comprehensive meteorological modeling system RAMS. Meteorol. Atmos. Phys. 49 (1-4), 69–91.
Pielke Sr., R.A., 2013. Mesoscale Meteorological Modeling, 3rd edition p. 98, International Geophysics Series.
Politis, E.S., Prospathopoulos, J., Cabezón, D., Hansen, K.S., Chaviaropoulos, P.K., Barthelmie, R.J., 2012. Modeling wake effects in large wind farms in complex terrain: the problem, the methods and the issues. Wind Energy 15 (1), 161–182.
Porté-Agel, F., Wu, Y.-T., Lu, H., Conzemius, R.J., 2011. Large-eddy simulation of atmospheric boundary layer flow through wind turbines and wind farms. J. Wind Eng. Ind. Aerodyn. 99, 154–168.
Prospathopoulos, J., Voutsinas, S.G., 2006. Implementation issues in 3D wind flow predictions over complex terrain. J. Sol. Energy Eng. 128 (4), 539–553.
Prospathopoulos, J., Cabezon, D., Politis, E.S., Chaviaropoulos, P.K, Rados, K.G., Schepers, J.C., Barthelmie, R.J., 2010. Simulation of wind farms in flat and complex terrain using CFD. In: TORQUE 2010 Conference, The Science Making Torque Wind. pp. 359–370.
Prospathopoulos, J., Politis, E.S., Rados, K.G., Chaviaropoulos, P.K., 2011. Evaluation of the effects of turbulence model enhancements on wind turbine wake predictions. Wind Energy 14 (2), 285–300.
Prospathopoulos, J.M., Politis, E.S., Chaviaropoulos, P.K., 2012. Application of a 3D RANS solver on the complex hill of Bolund and assessment of the wind flow predictions. J. Wind Eng. Ind. Aerodyn. 107–108, 149–159.
Richards, P.J., Hoxey, R., 1993. Appropriate boundary conditions for computational wind engineering models using the $k-\varepsilon$ turbulence model. J. Wind Eng. Ind. Aerodyn 46–47, 145–153.
Saad, Y., 2003. Iterative methods for sparse linear systems. Soc. Ind. Appl. Math., 49–50.
Salvador, R., Calbó, J., Milán, M., 1998. Horizontal grid size selection and its influence on mesoscale model simulations. J. Appl. Meteorol. 38 (9), 1311–1329.
Smagorinsky, J., 1963. General circulation experiments with the primitive equations. Mon. Weather Rev. 91 (3), 99–164.
Snyder, W.H., 1981. Guidelines for Fluid Modelling of Atmospheric Diffusion. Technical Report, EPA-600/8-81-009.. EPA Office of Air Quality, US
Taylor, P.A., 1976. Some numerical studies of surface boundary-layer flow over gentle topography. Bound.-Layer Meteorol. 11 (4), 439–465.
Trini Castelli, S., Ferrero, E., Anfossi, D., 2001. Turbulence closures in neutral boundary layers over complex terrain. Bound.-Layer Meteorol. 100 (3), 405–419.
Trini Castelli, S., Ferrero, E., Anfossi, D., Ohba, R., 2005. Turbulence closure models and their application in RAMS. Environ. Fluid Mech. 5 (1–2), 169–192.
Trini Castelli, S., Reisin, T.G., 2010. Evaluation of the atmospheric RAMS model in an obstacle resolving configuration. Environ. Fluid Mech. 10 (5), 555–576.
Troen, I., 1989. A high resolution spectral model for flow in complex terrain. In: Proceedings of the 9th Symposium on Turbulence and Diffusion. Roskilde, Denmark.
Von Bremen, L., 2007. Combination of deterministic and probabilistic meteorological models to enhance wind farm power forecasts. J. Phys. – Conf. Ser. 75, 012050.
Wilcox, D.C., 1988. Re-assessment of the scale-determining equation for advanced turbulence models. Am. Inst. Aeronaut. Astronaut. J. 26, 1299–1310.
Xue, M., Droegemeier, K.K., Wong, V., 2000. The advanced regional prediction system (ARPS) – a multiscale nonhydrostatic atmospheric simulation and prediction tool. Part I: model dynamics and verification. Meteorol. Atmos. Phys. 75, 161–193.
Xue, M., Droegemeier, K.K., Wong, V., Shapiro, A., Brewster, K., Carr, F., Weber, D., Liu, Y., Wang, D.H., 2001. The advanced regional prediction system (ARPS) – a multiscale nonhydrostatic atmospheric simulation and prediction tool. Part II: model physics and applications. Meteorol. Atmos. Phys. 76, 134–165.
Ying, R., Canuto, V.M., Ypma, R.M., 1994. Numerical simulation of flow data over two-dimensional hills. Bound.-Layer Meteorol. 70 (4), 401–424.
Ying, R., Canuto, V.M., 1995. Turbulence modeling over two-dimensional hills using an algebraic Reynolds stress expression. Bound.-Layer Meteorol. 77 (1), 69–99.
Ying, R., Canuto, V.M., 1997. Numerical simulation of flow over two-dimensional hills using a second order turbulence closure model. Bound.-Layer Meteorol. 85 (3), 447–474.
Young, G.S., Pielke, R.A., 1983. Application of terrain height variance spectra to mesoscale modeling. J. Atmos. Sci. 40 (10), 2555–2560.